Investigation of Acoustic Attenuation and Resonances in Lithium-Ion Batteries Using Ultrasound Spectroscopy

Simon Feiler,[a] Lukas Gold,[a] Sarah Hartmann,[a] and Guinevere A. Giffin*[a, b]

Ultrasound spectroscopy up to 6 MHz is carried out on a 12 Ah Lithium-ion battery pouch-cell. The analysis revealed that the attenuation behavior can be effectively described as having an absorption component and a resonance component. It was demonstrated that the absorption can be modeled as a second order polynomial. Two distinct resonances were identified at 2.2 MHz and 4.4 MHz. The first of these resonances shows a significant almost linear reduction in magnitude with increasing state of charge. By smartly choosing the ultrasound interrogation frequency to coincide with this resonance, an almost linear increase by a factor of more than five was measured in the signal amplitude between between state of charge levels of 0 and 100. This could provide the basis for a robust and straightforward state of charge determination method.

Introduction

Ultrasound has attracted increasing attention as a nondestructive diagnostic tool for investigation of lithium-ion batteries (LiBs). It has found potential application in the estimation of state of charge (SoC),[1–4] state of health (SoH)[5–9] and state of safety (SoS) by detecting plating[10] or thermal runaway[11] and thereby notice hazardous situations earlier. Ultrasound was not only utilized for operando measurements. It has also shown promising results in detecting production flaws[12,13] and to observe the wetting behavior[14] through ultrasound microscopy. While the application of ultrasound for assessing LiBs during operation and production has shown promising results, a comprehensive and systematic investigation into the frequency-dependent behavior of LiBs is missing. This hinders the optimization of ultrasound-based techniques for battery evaluation. This work aims to bridge this gap in understanding by systematically investigating the frequency-dependent attenuation behavior of ultrasound within lithium-ion batteries. Through an examination of the attenuation characteristics, a deeper understanding of the complex interplay between ultrasound waves and the intricate structures present within LiBs can be achieved. Ultimately, this knowledge can contribute to the development of more precise and effective ultrasound-based techniques.

In the sections that follow, different causes of ultrasound attenuation are outlined and an overview of the attenuation evaluation is given. The absorption part of the attenuation of a LIB is analysed at different SoC levels followed by the analysis of the first observed resonance at different SoCs.

Results and Discussion

Acoustic Attenuation

Attenuation is quantified by an attenuation coefficient $\alpha(f, x)$, commonly expressed in dB/m:

$$\alpha(f, x) = \alpha_0 \exp(-\alpha(f)x) \tag{1}$$

where x is the distance the sound wave travelled and α_0 and $\alpha(f, x)$ are the initial amplitude and the amplitude at the location of measurement, respectively. Acoustic attenuation can have multiple causes: beam spreading, scattering, absorption and resonant reflection. Acoustic beam spread refers to the phenomenon that an acoustic wave gradually expands and becomes broader as it propagates through a medium. A distinction between the far field and the near field has to be made. The end of the near field N can be approximated by:

$$N = \frac{D^2 - \lambda^2}{4\lambda} \tag{2}$$

where λ is the wavelength and D the diameter of the transducer. In the near field, the beam spread is negligible while in the far field a quadratic weakening of the beam energy is observed.[15]

Scattering phenomena occur in non-homogeneous materials, caused by sudden shifts in acoustic impedance at boundaries or interfaces due to differences in density or sound velocity. Such deviations can arise from foreign inclusions, the presence of gas-filled pores, inherent material imperfections, or

[a]   S. Feiler, Dr. L. Gold, Dr. S. Hartmann, Dr. G. A. Giffin
      Fraunhofer R&D Center Electromobility Fraunhofer
      Institute for Silicate Research
      Neunerplatz 2, 97082 Würzburg (Germany)
      E-mail: guinevere.giffin@isc.fraunhofer.de

[b] Dr. G. A. Giffin
      Julius-Maximilians-Universität Würzburg (JMU)
      Faculty of Chemistry and Pharmacy
      Chemical Technology of Materials Synthesis
      Röntgenring 11, 97070 Würzburg (Germany)

Batteries & Supercaps

Research Article
doi.org/10.1002/batt.202400212

Chemistry Europe
European Chemical
Societies Publishing

materials comprised of discrete particles.[15] The relevance of scattering effects hinges on the relationship between the wavelength λ of the acoustic wave and the characteristic dimensions of the microstructure of the material. Specifically, Rayleigh scattering occurs when the wavelength λ is larger than the characteristic size of these microstructures. Rayleigh scattering is characterized by a quartic frequency dependency, $\alpha_{Rayleigh} \propto f^4$. In practice, wave scattering effects are negligible in the low megahertz (MHz) frequency range, when λ exceeds ten times the characteristic size.[15,16] Other forms of scattering, such as stochastic or diffusion scattering, become significant at even higher frequencies.

Absorption is the direct conversion of sound energy into heat within a material. This occurs due to dislocation damping, hysteresis, thermoelastic effects and viscous displacement. These absorption mechanisms can often be effectively captured and modeled using second-order polynomial expressions:[17,18]

$$\alpha(f) = af + bf^2 \tag{3}$$

Resonance or rather resonant reflection occurs when the frequency of an external force matches the natural frequency, or a higher harmonic, of the system. In the context of layered structures, the layering distance d and sound velocity c defines the natural frequency f_n of the material as:

$$f_n = \frac{c}{2d} \tag{4}$$

Excitation at this frequency leads to a resonant reflection, meaning all the reflected waves constructively interfere, leading to an overall increase in reflection and therefore a decreased transmission. This phenomenon is located at a frequency band around the natural frequency, which is why it can be referred to as a band gap and is conceptionally equivalent to band gaps in solid-state physics.

Principle of Attenuation Measurements

In this section, the concept of an attenuation measurement is outlined. The method is based on the principles and formulae introduced by Lee et al.[19] All parameters are expressed in terms of wave amplitude; for an expression in intensity, the amplitude has to be squared. In general, the frequency-dependent attenuation of a sample is calculated by analyzing the amplitude spectrum of the transmission through the measurement setup with the sample, divided by the transmission spectrum of the setup alone. This way the influence of the transducers and delay lines (DL) cancels out and only the amplitude response of the sample, in this case, a battery cell remains. By design, the pulses driving the transducer were short enough in time domain, that they can be selected by a windowing function and do not superimpose with reflections from the delay line or back wall echo of the cell. More detail on the design of the experiment can be found in Section "Experimental".

If $U(t)$ is the pulse that drives the transducer its Fourier transform and the inverse can be written as:

$$U(f) = \int_{-\infty}^{\infty} U(t)\exp(-ift)dt$$
$$U(t) = \frac{1}{2\pi} \int_{-\infty}^{\infty} U(f)\exp(-ift)df \tag{5}$$

For the setup containing the cell, the expression for the received signal amplitude in Fourier space $U_{sample}(f)$ by transducer 2, is as follows:

$$U_{sample}(f) = A_1(f)\exp[(-\alpha_{DL}(f) - i\beta_{DL}(f))L_{DL}]$$
$$t_{DL,Bat}\exp[(-\alpha_{Bat}(f) - i\beta_{Bat}(f))L_{Bat}]t_{Bat,DL}$$
$$\exp[(-\alpha_{DL}(f) - i\beta_{DL}(f))L_{DL}]A_2(f)U(f) \tag{6}$$

where $A_1(f)$ and $A_2(f)$ is the frequency response of transducer 1 and 2, respectively. $\alpha_{DL}(f)$ and $\beta_{DL}(f)$ multiplied by the length of the delay line L_{DL} are the attenuation and phase shift caused by the delay line. Similarly $\alpha_{Bat}(f)$ and $\beta_{Bat}(f)$ multiplied by the thickness of the battery L_{Bat} are the attenuation and phase shift caused by the battery. $t_{DL,Bat}$ is the transmission coefficient from the delay line into the battery and $t_{Bat,DL}$ vice versa. In general, the transmission coefficient $t_{M_i,M_{i+1}}$ at an interface between two materials M_i and M_{i+1} is defined as:

$$t_{M_i,M_{i+1}} = \frac{2Z_{M_{i+1}}}{Z_{M_i} + Z_{M_{i+1}}} \tag{7}$$

and the reflection coefficient $r_{M_i,M_{i+1}}$ at the interface of Material M_i to Material M_{i+1} is defined as:

$$r_{M_i,M_{i+1}} = \frac{Z_{M_{i+1}} - Z_{M_i}}{Z_{M_i} + Z_{M_{i+1}}} \tag{8}$$

where Z_{M_i} is the acoustic impedance of Material M_i, defined as the product of density ρ_{M_i} and sound velocity c_{M_i}:

$$Z_{M_i} = \rho_{M_i}c_{M_i} \tag{9}$$

Without the battery in the setup, the following equation is obtained:

$$U_{empty}(f) = A_1(f)\exp[(-\alpha_{DL}(f) - i\beta_{DL}(f))L_{DL}]t_{DL,DL}$$
$$\exp[(-\alpha_{DL}(f) - i\beta_{DL}(f))L_{DL}]A_2(f)U(f) \tag{10}$$

where $t_{DL,DL}$ is the transmission coefficient from one delay line to the other. Dividing the measured spectra of the setup with and without the cell, i.e. dividing Eq. (6) by Eq. (10), yields the frequency response of the battery, if noise is neglected:

$$U_{Bat}(f) \approx \frac{U_{sample}(f)}{U_{empty}(f)}$$
$$= \frac{t_{Bat,DL}t_{DL,Bat}}{t_{DL,DL}}\exp[(-\alpha_{Bat}(f) - i\beta_{Bat}(f))L_{Bat}] \tag{11}$$

Batteries & Supercaps

Research Article
doi.org/10.1002/batt.202400212

Chemistry Europe
European Chemical
Societies Publishing

The frequency response can be split into amplitude response $A_{Bat}(f)$ and phase response $\varphi_{Bat}(f)$:

$$U_{Bat}(f) = |U_{Bat}(f)|\exp(i\arg(U_{Bat}(f)))$$
$$= A_{Bat}(f)\exp(i\varphi_{Bat}(f)) \tag{12}$$

where arg is the argument of the complex number $U_{Bat}(f)$. $A_{Bat}(f)$ and $\varphi_{Bat}(f)$ can be identified as:

$$A_{Bat}(f) = \frac{t_{Bat,DL}t_{DL,Bat}}{t_{DL,DL}}\exp[-\alpha_{Bat}(f)L_{Bat}]$$
$$\varphi_{Bat}(f) = -\beta_{Bat}(f)L_{Bat} \tag{13}$$

The attenuation coefficient of the battery $\alpha_{Bat}(f)$ can be obtained by solving $A_{Bat}(f)$ for $\alpha_{Bat}(f)$:

$$\alpha_{Bat}(f) = -\frac{1}{L_{Bat}}\log\left[\frac{t_{DL,DL}}{t_{Bat,DL}t_{DL,Bat}}\left|\frac{U_{sample}(f)}{U_{empty}(f)}\right|\right]20\ \text{dB} \tag{14}$$

$t_{Bat,DL}t_{DL,Bat}$ can further be simplified to $1 - r^2_{DL,Bat}$ through simple arithmetic by using the explicit expressions for the reflection and transmission coefficients, as in Eq. (7) and Eq. (8). $r_{DL,Bat}$ was calculated to be around 3% and measured to be around 5%, refer to Section "Reflection Coeffcient from Delay Line to Cell" and Figure S4 in the supporting information. Therefore $1 - r^2_{DL,Bat} > 99.7\%$ is close enough to 1 to be neglected. $t_{DL,DL}$ should theoretically be 1 since the delay lines are made from the same material but can deviate due to coupling issues. It was verified experimentally that it is close enough to 1 to be neglected. Therefore, the attenuation of the battery can be described by the simplified term:

$$\alpha_{Bat}(f) = -\frac{1}{L}\log\left[\left|\frac{U_{sample}(f)}{U_{empty}(f)}\right|\right]20\ \text{dB} \tag{15}$$

Figure 1 shows two measurements with center frequencies of 0.35 MHz and 1.7 MHz. The wave forms in time domain for the empty setup and setup with sample are shown in (a), the amplitude responses are shown in (b) and the attenuation, calculated according to Eq. (15), is depicted in (c). The attenuation is calculated piecewise. One piece stems from a single measurement at a certain center frequency, spanning a small frequency range which is depicted as one line section in (c). The sections corresponding to the measurements at 0.35 and 1.7 MHz are colored cyan and blue. Figure 1 exemplifies the attenuation calculations. In the next section, the same method is employed to calculate attenuation across a wider frequency range.

Interpretation of Attenuation Results

In this section, the attenuation measurements of the battery cell at different SoCs are interpreted and the causes of the attenuation, as outlined in Section "Acoustic Attenuation" are discussed. The results of the attenuation measurements can be seen in Figure 2 (SOCs are color-coded). Scattering can be neglected as the wavelengths are large compared the components of the battery cell. An analysis to estimate the impact of beam broadening was conducted. The effect of beam broadening can be interpreted as a change in the solid angle of the empty measurement and the measurement with cell. A smaller solid angle is present when measuring the empty setup, therefore the energy of the pulse appears larger. This can be accounted for by a beam broadening correction factor C:
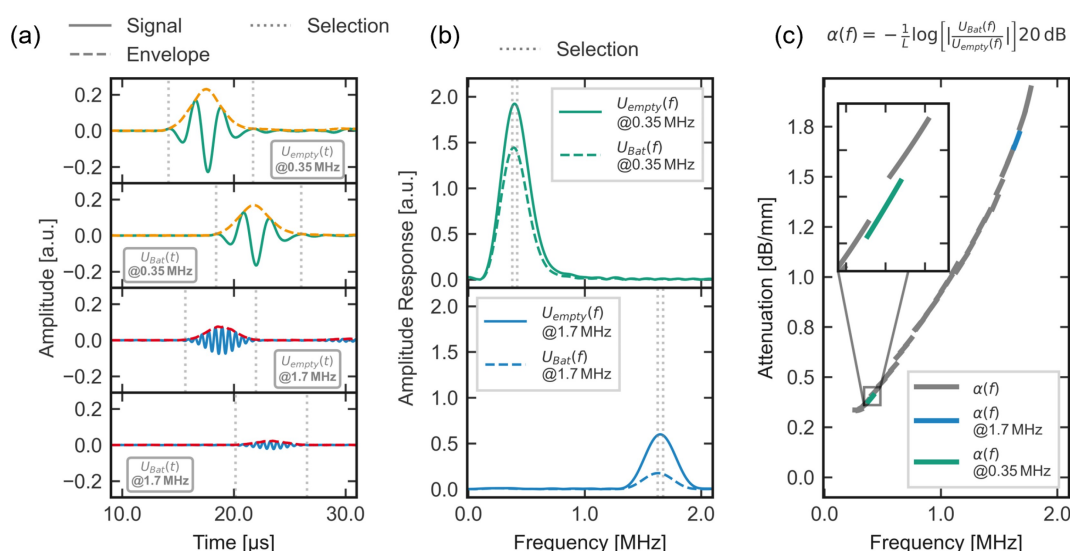

Figure 1. Attenuation measurement principle using Morlet wavelets with various center frequencies. Panel (a) displays signal comparisons between an empty setup and a setup with a battery in time domain. The Fourier transform of the first arrival (selection in (a)) is shown in the panel (b). From the Fourier transform, the attenuation per length can be calculated by division of $U_{Batt}(f)$ and $U_{empty}(f)$. The attenuation coefficient is shown in (c). For each time-signal attenuation coefficients around its center frequency (selection in (b)) were evaluated. Multiple time-signals with different center frequencies result in a spectra with a broader frequency range.
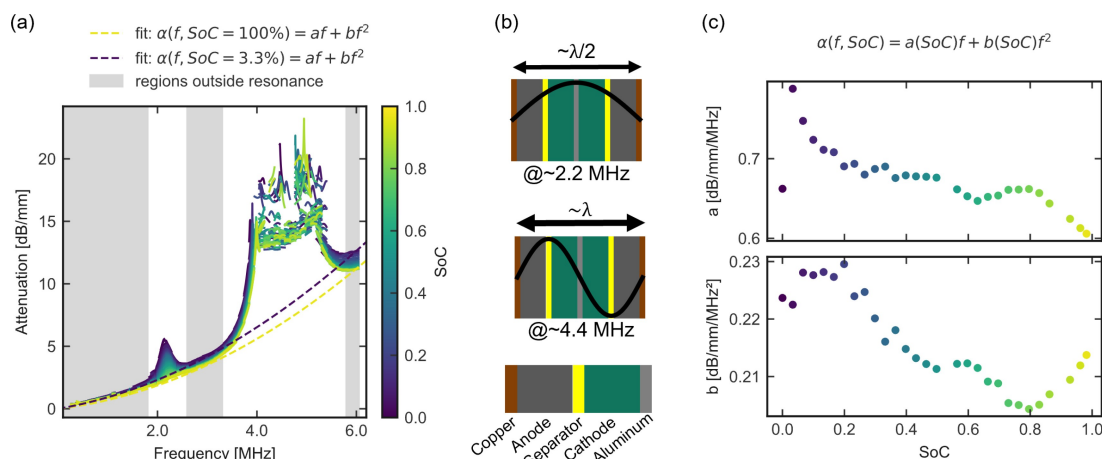
Figure 2. Panel (a) displays the attenuation coefficients of a 12 Ah Kokam lithium-ion battery over frequencies at different SoCs, showcasing the frequency-dependent behavior. Regions dominated by absorption (conversion of sound energy into heat) are shaded gray. The white regions are dominated by resonant behavior arising from the layered structure of the battery. Resonances occur when the wavelength matches the periodicity of the battery layers, this is visualized in (b). The absorption regions are fitted using a second-order polynomial with the dashed lines in (a) representing the SoC levels 3.3 % and 100 %. The results of the fitting process in (c) show a clear dependency of absorption on SoC.

$$C = \frac{\Omega_{empty}}{\Omega_{sample}} = \frac{r^2\pi/4\pi R_{empty}^2}{r^2\pi/4\pi R_{sample}^2} = \frac{R_{sample}^2}{R_{empty}^2} \qquad (16)$$

where Ω_{empty} and Ω_{sample} are the solid angles of the empty setup and setup with sample respectively. r is the radius of the transducer disk, R_{empty} is the distance from the sender to the receiver in the empty setup and R_{sample} the distance from the sender to the receiver in the setup with sample. In our case $R_{empty} = 30.0$ mm and $R_{sample} = 36.4$ mm, therefore $C = 1.47$. This corresponds to 1.67 dB and therefore would lead to a correction of 1.67 dB/6.4 mm = 0.261 dB/mm. At the higher frequencies ($f > \approx 4$ MHz) the receiver is in the near field of the receiver, and thus beam broadening can be ignored.[15] For lower frequencies, the receiver is located in the far field and therefore subject to a quadratic decrease in pressure amplitude. This effect will not be corrected for since it is unclear how exactly to correct for beam broadening in the transition region between near and far field. Its effect however is small compared to the absolute values of the attenuation and should not obscure any underlying effects. It should however be be noted that the attenuation coefficients at lower frequencies could be overestimated by up to a maximum of this factor.

The remaining attenuation effects, i.e. resonant reflection and absorption, as detailed in Section "Acoustic Attenuation" will now be examined. Figure 2(a) depicts the attenuation calculated from a set of measurements over the whole SoC range and a broad frequency range. Different attenuation regimens can be recognized. In particular, two frequency ranges from 1.8 to 2.6 MHz and from 3.3 to 5.8 MHz stand out, where the attenuation deviates from the underlying background. Deviations in these ranges can be attributed to resonances where the wavelength matches the periodicity of the battery layers shown in Figure 1(b). The first resonance can be attributed to a resonant unit consisting of two active cell units, i.e. spanning from copper to copper layer, depicted in the top of Figure 1(b). In total the battery cell consists of 34 active cell

units, one active cell is depicted at the bottom of Figure 1(b). The second resonance at higher frequency can be attributed to a resonant unit consisting of one active cell unit, i.e. from copper to aluminum layer. The attenuation caused by the second resonance is not fully resolved as the attenuation in the vicinity of this resonance was so large that no signal could be detected. The noise recorded sets a lower limit on the attenuation, i.e. ≈ 13 dB/mm, which can be seen in the noisy data between ≈ 4 MHz and ≈ 5.2 MHz. The resonances will be discussed in greater detail in the next section. In this section, the regions outside the resonances, marked in gray, will be analyzed. As discussed above, the other attenuation mechanisms, i.e. scattering, beam broadening and resonances, can be ruled out, and the attenuation in these regions should purely be caused by absorption. Therefore, a second order polynomial is fitted to the data at each SoC. The coefficients of the polynomial are shown as a function of SoC in Figure 2(c) as described by Eq. (3). The linear term (coefficient a) of absorption clearly depends on SoC, as was already found by Meng et al.[20] However, unlike Meng et al., no strictly linear dependency of a(SoC) with the SoC was detected here. In contrast, there a plateau in a(SoC) between 20 and 80 % SoC. The quadratic absorption term, b(SoC), does not show a trend that can easily be interpreted. It increases until 20 % SoC then decreases until 80 % SoC and then increased again. Similar effects were also observed in another cell type, as shown in Figure S7 in the supporting information.

Resonance

This section analyzes the first peak in Figure 2(a) in greater detail and in particular its dependency on SoC. The resonance at 2.2 MHz is where the wavelength matches the periodicity of two active battery cell units depicted in the upper panel of Figure 2(b). The enhancement of the reflection in this frequency

Batteries & Supercaps

Research Article
doi.org/10.1002/batt.202400212

Chemistry Europe
European Chemical
Societies Publishing

range is a strong indication that this peak in the attenuation is indeed resonant reflection, see Figure S4 in the supporting information. At a frequency of 2.2 MHz, the reflection coefficient in Figure S4 is the largest at lower SoCs and then gradually decreases as the resonance decreases for increasing SoCs.

For the purpose of studying the resonance in isolation, the absorption background, described by the second order polynomial, was subtracted from the data. The results can be seen in Figure 3(a). The resonance shifts to higher frequencies for higher SoCs and vanishes at high SoCs. To quantify these effects, Lorentz curves $L(f, A, f_0, \gamma)$ were used to fit the data to extract the height A, position f_0 and width γ of the resonance.

$$L(f, A, f_0, \gamma) = A \frac{1}{1 + \left(\frac{(f-f_0)}{\gamma}\right)^2} \tag{17}$$

The coefficients of the fit are shown in Figure 2(b). There is a correlation of the magnitude and position of the resonance with SoC. The almost linear shift in resonance frequency can be explained by the almost linear shift in sound velocity with SoC of the cell as a whole, as was described in, e. g. Ref. [21]. A larger sound velocity leads to a larger wavelength at a given frequency, therefore a higher frequency is required in order to satisfy the resonance condition. During charging, the layering distance of the periodic structure of the LIB increases with SoC, due to the expansion of the graphite anode, causing an opposing effect. This expansion effect plays a minor role since the thickness only increases by approximately 2% while the sound velocity increases by around 5%.[21] The largest change can be observed in the height of the resonance. From fully discharged to fully charged, the attenuation of the resonance decreases by around 3 dB/mm until the resonance almost vanishes. For the entire cell, this is nearly 20 dB which

corresponds to a factor of 10 in signal amplitude. Additionally, the change is fairly linear. The scenario where the resonance vanishes with this cell type is a result of its specific composition. For another cell with a slightly different cell chemistry, the resonance shows the same qualitative behavior but does not vanish at high SoCs, see Figure S8 in the supporting information.

The decrease in the magnitude of the resonance can be attributed to two factors. Firstly, the decrease in reflectivity of the copper graphite interface at higher lithiation degree. Secondly, the increase in reflectivity of the aluminum NCM interface at lower lithiation degree of the cathode. These factors suppress this specific resonance by decreasing the reflection at the boundaries and increasing the reflection at the center of the resonator, as depicted in Figure 2(b). The changes in reflectivity are caused by changes in the Young's modulus of the active material that causes changes in the speed of sound. A lower speed of sound leads to a lower acoustic impedance, see Eq. (9), and therefore to a higher reflection coefficient, see Eq. (8), as the acoustic impedance of the metal current collectors is an order of magnitude larger than that of the active material. The Young's modulus of NCM during delithiation decreases,[22] therefore the 100% SoC cathode exhibits a lower sound velocity than the 0% SoC cathode. Likewise, the Young's modulus, i.e. the stiffness, of the graphite increases during lithiation.[23]

The substantial decrease in attenuation with SoC provides an opportunity to create a cost-effective and straightforward SoC estimation system. This can be achieved by strategically choosing the US interrogation frequency to align with the cell's first resonance frequency. This can be done by choosing a transducer with an appropriate center frequency or electrically driving the transducer to align with the cell's resonant frequency. The latter approach is depicted in Figure 4, where
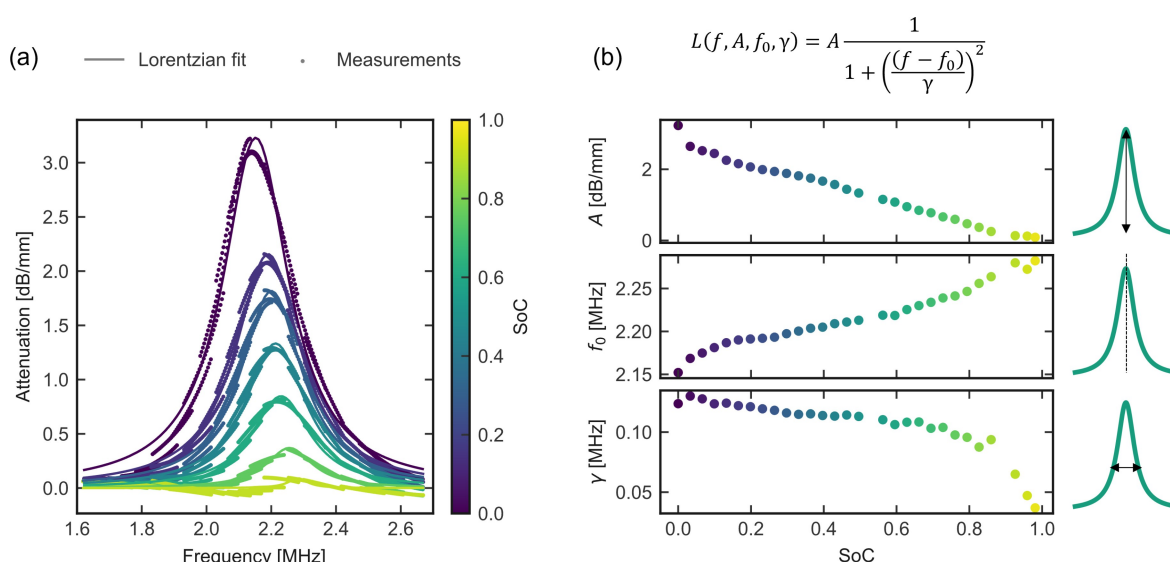

Figure 3. Attenuation coefficient at the first resonance of a 12 Ah Kokam lithium-ion battery at various SoCs. Panel (a) shows the attenuation coefficient in the region of the first resonance after subtracting the second order polynomial fit that models absorption. For feature extraction, Lorentzians are fitted to the data. The results can be seen in (b). The height of the resonance is changing almost linearly with SoC due to changes in sound velocity and density of the active materials. The center frequency shifts to higher frequencies due to an increase in the cell's overall sound velocity at higher SoCs.
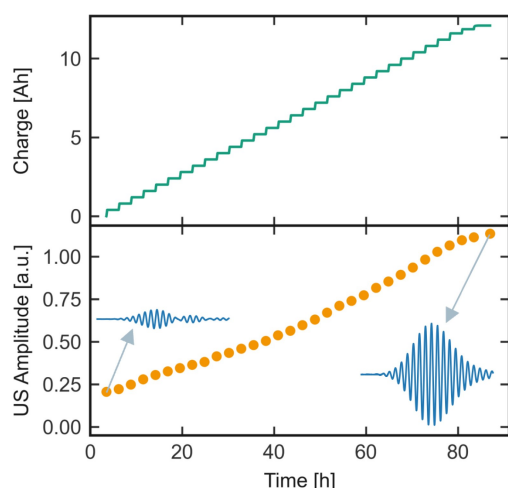
Batteries & Supercaps

Research Article
doi.org/10.1002/batt.202400212

Chemistry Europe
European Chemical
Societies Publishing

Figure 4. Charge and measured ultrasound amplitude at 2.2 MHz of a 12 Ah Kokam lithium-ion battery during the GITT-like charge cycle. The ultrasound transmission signals at 0% and 100% SoC are are shown in blue. This graph illustrates the application of the finding that the attenuation at the first resonance frequency depends on the state of charge.

the transducer was driven with a Morlet wavelet with a center frequency of 2.2 MHz. Multiple charge and discharge cycles are depicted in Figure S5. The US amplitude exhibits a strong correlation with SoC as predicted by the attenuation behavior. The amplitude increases by more than a factor of 5. This attenuation effect is more pronounced than the change in the time of flight (ToF) that has been previously been used to determine SoC.[1–3] For comparison, the ToF change is only on the magnitude of 5%.[21] Therefore, measuring the signal amplitude at the first resonance frequency instead of ToF could prove to be more robust and straightforward, which could allow a low cost setup to be developed. Nonetheless, the robustness of the method still needs to be demonstrated during a continuous charge, over the course of aging and at different temperatures in future experiments.

Conclusions

An innovative attenuation measurement technique utilizing Morlet wavelets was introduced to achieve a good signal to noise ratio at a given frequency while avoiding interference of back wall echos with the signal. Attenuation measurements were conducted at various SoCs across a wide range of frequencies up to 6 MHz. The various factors contributing to attenuation were evaluated. Beam broadening and scattering were deemed negligible. A second order polynomial fit effectively captures the absorption behavior of the cell. The extracted absorption coefficients offer valuable insights for the design and dimensioning of future experimental setups for thicker cells or cell stacks, including the extrapolation to higher frequencies beyond those measured in this study. Two resonance regions were identified. The first resonance can be attributed to a resonant unit made up of elements which belong to two active cells, i.e., spanning from copper to copper

layer. The second resonance at higher frequency can be attributed to a resonant unit consisting of one active cell, i.e., from copper to aluminum layer. The resonance frequency of the first resonance increases with SoC which can be attributed to an increase in stiffness and therefore sound velocity of the higher lithiated graphite anode. The magnitude of the resonance also depends on SoC which can be attributed to the decrease in reflectivity of the copper-graphite interface at higher lithiation degree and the increase in reflectivity of the aluminum-NCM interface at lower lithiation degree of the cathode. The substantial decrease in attenuation with SoC could be used for SoC estimation in a cheap and easy to implement setup when smartly choosing the frequency of the transducers to coincide with this first resonance of the cell.

Experimental

Battery Specifications

Lithium-ion batteries (LIBs) with a nominal capacity of 12 Ah, of type SLPB065070180 from Kokam Co., Ltd were employed. These batteries feature 17 double sided graphite anode, 16 double sided and two single sided nickel-rich NCM cathode. While the precise composition of the electrolyte is not provided in the datasheet, it is known to comprise lithium hexafluorophosphate ($LiPF_6$) dissolved in a mixture of ethylene carbonate (EC) and ethyl methyl carbonate (EMC). The active area of the electrodes measure 67 mm×165 mm.

Electrochemical Testing

Electrochemical testing was performed using a SP-240 by BioLogic Sciences Instruments. 0% SoC is prepared by a constant voltage (CV) hold at 2.7 V, which lasted for 2 hours. Subsequently, a galvanostatic intermittent titration technique (GITT)-like measurement was executed. The resulting voltage profile is depicted in Figure 5 in the top panel. It consists of multiple 10 minute charging
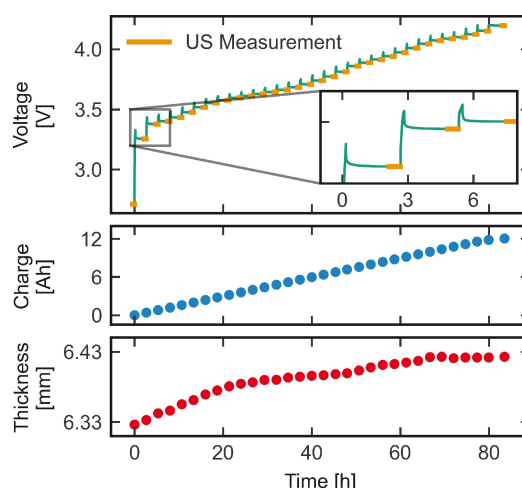

Figure 5. Electrochemical preparation of the SoC and dilation measurements. The voltage profile of the GITT-like measurement is shown in the top panel. Each 10 minute charge step at C/5 is followed by a 2 h 30 min break. In the last 30 min of the pause, the ultrasonic measurements are conducted. The charge and thickness of the cell at the time of measurement is shown in the middle and bottom panel, respectively.

Batteries & Supercaps

Research Article
doi.org/10.1002/batt.202400212

Chemistry Europe
European Chemical
Societies Publishing

steps at a rate of C/5, each followed by a 2 hour and 30 minute relaxation step. Each charge step contributed 400 mAh, approximately 3.3% of the SoC. After 30 charge steps, a one hour long CV step at 4.2 V was executed to prepare 100% SoC.

Experimental Setup

A sketch and image of the experimental setup is shown in Figure 6. The cell was subjected to an external pressure of 25 kPa. This pressure was applied using two springs (with a spring constant of 17.65 N/mm, model number 13000, from SODEMANN Industrifjedre A/S) to ensure pressure control within a ± 1 kPa range. A pressure sensor (KM38-1 kN load cell, ME-Systeme GmbH) was employed to accurately measure the force exerted on the battery cell. To facilitate a uniform pressure distribution, the cells were positioned between two 15 mm thick PMMA plates that also serve as delay lines. PMMA was chosen because of its acoustic properties. The acoustic impedance of PMMA is close to the one of LIBs therefore ideal coupling is granted and losses due to reflection are minimized. The improved coupling compensates for the higher absorption of the PMMA, e.g., when compared with aluminum. Two transducers were mounted on the PMMA bracings and coupled accousitcally via canola oil. The acoustic coupling at the interface of battery and PMMA delay line was improved by canola oil as well.

Ultrasonic Measurements

During the final 30 minutes of the 2 hour and 30 minute break period, the ultrasound measurements were conducted as depicted in Figure 5. The thickness of the cell was continuously monitored using a laser dilation sensor (IL-S065, KEYENCE DEUTSCHLAND GmbH) coupled with an amplifier unit (IL-1000, KEYENCE DEUTSCHLAND GmbH). The thickness of the cell at the time of the ultrasound measurement is illustrated in Figure 5.

For the measurements, Morlets wavelets were utilized:

$$M(t) = \pi^{-0.25} \exp(i2\pi f_0 t)\exp\left(-\frac{1}{2}\frac{t^2}{\sigma^2}\right) \tag{18}$$

where σ^2 is the width and f_0 the center frequency of the Morlet. Morlet wavelets were chosen over spike and sine excitation methods for several reasons. Spike excitations exhibit a spectral

density that is low for frequencies outside the transducer's center frequency. This would result in a diminished signal-to-noise ratio, and given the highly attenuative nature of the battery cell, could potentially yield inadequate results. Morlet wavelets were chosen instead of sine excitation to avoid interference with the reflections stemming from delay lines and frontwall-backwall echoes. Morlet wavelets offer the advantage of precise adjustments in both bandwidth and signal width, allowing for more controlled measurements. Morlet waveforms were generated with a bandwidth (full width half max (FWHM)) of 294 kHz and a pulse width (FWHM) of 3 μs. For the spectroscopy, the center frequency was varied in 50 kHz steps from waveform to waveform. Three different transducers were utilized. The ultrasonic transducers (U2P10,U5P10, United NDT GmbH) had a nominal center frequency of 2.0 MHz, 5 MHz and a diameter of 10 mm, while a V603 from Olympus had a nominal center frequency of 1 MHz and a diameter of 13 mm.

For the generation of Morlet waveforms an arbitrary wave form generator TGP3151 (Aim TTi) was interfaced via python VISA. Those signals were amplified by a broadband high frequency amplifier Hubert A1020-75-250 up to 100 V. With the U5P10 connected, the 100 V could not be reached due to the 75 W limitation of the amplifier. Signals were recorded by an oscilloscope (WaveSurfer HD by Teledyne LeCroy) at a sampling rate of 500 MS/s. Signals were averaged over 1024 shots.

Conflict of Interests

The authors declare no conflict of interest.

Data Availability Statement

The data that support the findings of this study are available from the corresponding author upon reasonable request.

Keywords: lithium-ion battery · ultrasonic resonance · Ultrasound spectroscopy · layered structure · state of charge
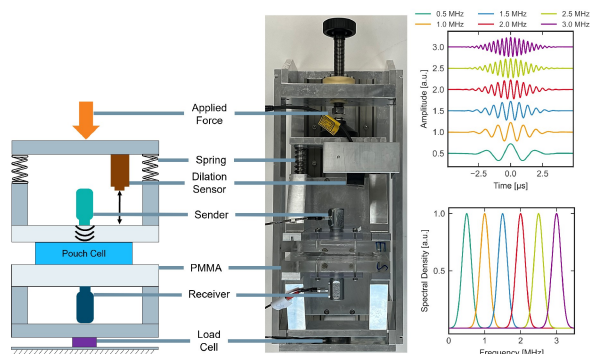

Figure 6. Schematic and image of experimental setup and exemplary excitation signals. A schematic of the measurement setup is shown on the left. The cell is braced between two polymethyl methacrylate (PMMA) plates with transducers affixed to the bracing. The pressure and cell thickness are measured at all times. On the right exemplary Morlet excitation signals are shown in time and frequency domain.

[1] A. G. Hsieh, S. Bhadra, B. J. Hertzberg, P. J. Gjeltema, A. Goy, J. W. Fleischer, D. A. Steingart, *Energy Environ. Sci.* **2015**, *8*, 1569.
[2] L. Gold, T. Bach, W. Virsik, A. Schmitt, J. Müller, T. E. Staab, G. Sextl, *J. Power Sources* **2017**, *343*, 536.
[3] P. Ladpli, F. Kopsaftopoulos, F.-K. Chang, *J. Power Sources* **2018**, *384*, 342.
[4] H. Sun, P. Ramuhalli, R. Amin, I. Belharouak, *Appl. Phys. Lett.* **2024**, *124*.
[5] K. W. Knehr, T. Hodson, C. Bommier, G. Davies, A. Kim, D. A. Steingart, *Joule* **2018**, *2*, 1146.

Batteries & Supercaps

Research Article
doi.org/10.1002/batt.202400212

Chemistry Europe
European Chemical
Societies Publishing

[6] C. Bommier, W. Chang, J. Li, S. Biswas, G. Davies, J. Nanda, D. Steingart, *J. Electrochem. Soc.* **2020**, *167*, 020517.

[7] Y. Wu, Y. Wang, W. K. C. Yung, M. Pecht, *Electronics* **2019**, *8*, 751.

[8] J.-Y. Kim, J.-H. Jo, J.-W. Byeon, *Microelectron. Reliab.* **2020**, *114*, 113859.

[9] M. Webster, E. Frankforter, A. Zuercher, S. Deshpande, W.-C. A. Lam, D. Caicedo, B. De Mattia, Y. Lin, D. Perey, *J. Power Sources* **2024**, *606*, 234552.

[10] C. Bommier, W. Chang, Y. Lu, J. Yeung, G. Davies, R. Mohr, M. Williams, D. Steingart, *Gel Rep. Phys. Sci.* **2020**, *1*, 100035.

[11] M. C. Appleberry, J. A. Kowalski, S. A. Africk, J. Mitchell, T. C. Ferree, V. Chang, V. Parekh, Z. Xu, Z. Ye, J. F. Whitacre, S. D. Murphy, *J. Power Sources* **2022**, *535*, 231423.

[12] D. Wasylowski, N. Kisseler, H. Ditler, M. Sonnet, G. Fuchs, F. Ringbeck, D. U. Sauer, *J. Power Sources* **2022**, *521*, 230825.

[13] L. Pitta Bauermann, J. Münch, M. Kroll, S. Enghardt, M. Vetter, *Energy Technol.* **2023**, *14*, 2300323.

[14] Z. Deng, Z. Huang, Y. Shen, Y. Huang, H. Ding, A. Luscombe, M. Johnson, J. E. Harlow, R. Gauthier, J. R. Dahn, *Joule* **2020**, *4*, 2017.

[15] J. Krautkrämer, H. Krautkrämer, *Ultrasonic testing of materials*, Springer-Verlag, Berlin and Heidelberg, 4th fully revised edition, translation of the 5th revised german edition edition **1990**.

[16] E. P. Papadakis, *J. Acoust. Soc. Am.* **1965**, *37*, 711.

[17] G. L. Workman, D. Kishoni, P. O. Moore (Editors), *Ultrasonic testing*, Vol. 7 of *Nondestructive testing handbook*, American Society for Nondestructive Testing, Columbus, Ohio, 3. ed. **2007**.

[18] K. Ono, Applied *Sciences* **2020**, *10*, 2230.

[19] C. C. Lee, M. Lahham, B. G. Martin, *IEEE Trans. Ultrasonics, Ferroelectrics, Frequency Control* **1990**, *37*, 286.

[20] K. Meng, X. Chen, W. Zhang, W. Chang, J. Xu, *J. Power Sources* **2022**, *547*, 232003.

[21] S. Feiler, P. Daubinger, L. Gold, S. Hartmann, G. A. Giffin, *Batteries & Supercaps* **2023**, *6*, e202200518.

[22] R. Xu, H. Sun, L. S. de Vasconcelos, K. Zhao, *J. Electrochem. Soc.* **2017**, *164*, A3333.

[23] Y. Qi, H. Guo, L. G. Hector, A. Timmons, *J. Electrochem. Soc.* **2010**, *157*, 558.